A multi-scale analysis method for catalyst layers in PEMFC catalyst coated membranes: Correlation of catalyst layer microstructure with dispersion recipes and hot-press pressure

Ahammed Suhail Odungat,[1] Lars Grebener,[1] Oliver Pasdag,[2] Thai Binh Nguyen,[4,5] Yawen Zhu,[1] Sebastian Kohsakowski,[3] Ivan Radev,[2,6] Fatih Özcan,[1,4] Doris Segets[1,4,z]

[1] Institute for Energy and Material Processes – Particle Science and Technology (EMPI-PST), University of Duisburg-Essen, Duisburg, Germany
[2] ZBT GmbH – The Hydrogen and Fuel Cell Center, Duisburg, Germany
[3] Laufenberg GmbH, Krefeld, Germany
[4] CENIDE – Center for Nanointegration Duisburg-Essen, Germany
[5] Interdisciplinary Center for Analytics on the Nanoscale (ICAN), University of Duisburg-Essen, Duisburg, Germany
[6] Institute of Electrochemistry and Energy Systems – Academician Evgeni Budevski, Bulgarian Academy of Sciences, Bulgaria
[z] Corresponding author doris.segets@uni-due.de

Abstract

This study introduces a comprehensive multi-scale framework for analyzing and optimizing the microstructural properties of catalyst-coated membranes (CCMs) in polymer electrolyte membrane fuel cells (PEMFCs). The approach integrates mercury intrusion porosimetry (MIP), multiple microscopy techniques, and non-destructive focused ion beam scanning electron microscopy (FIB-SEM), enabling detailed characterization across microstructural scales, from tens of nanometers to hundreds of micrometers. A custom MATLAB-based image-processing algorithm was developed to extract pore attributes—including size, porosity, and geometry—from FIB-SEM cross-sections, providing unprecedented insights into microstructural variations under varying fabrication conditions. By employing this multi-scale analysis, the study revealed significant correlations between process parameters (such as hot-pressing) and dispersion formulations with the resulting microstructural properties and electrochemical performance. The study revealed previously hidden dependencies, demonstrating that catalyst layers produced from different dispersions exhibit distinct responses to hot-pressing and further elucidating the critical interplay between pore structure, internal resistance, and adhesion in achieving CCMs with optimal performance. This novel approach provides a scalable, cost-effective tool for probing CCM structure-property-performance correlations. By enabling the characterization of both surface and internal features within catalyst layers, our method lays the foundation for rational, data-driven design of CCMs and other electrochemical systems, such as proton exchange membrane electrolyzers.

Keywords

Proton exchange membrane fuel cell; catalyst coated membrane; catalyst layers; microstructure

1. Introduction

PEMFCs hold significant potential for transitioning from conventional fossil fuels to greener energy alternatives. However, the high cost of raw materials, stability, and durability of electrodes have hindered their widespread adoption despite decades of technological development [1–4]. It is estimated that approximately 60 % of fuel cell production costs are attributed to the membrane electrode assembly (MEA), which is known as the heart of the fuel cell, where the electrochemical reactions occur [5,6]. This high cost is largely due to the use of expensive and precious metals, such as platinum (Pt), as electrocatalyst [7–9]. The inefficiency of the cathodic oxygen reduction reaction (ORR) further exacerbates costs, necessitating additional catalyst material at the cathode side of the MEA. Two main factors that contribute to this inefficiency are the sluggish kinetics of the ORR and mass transport limitations [9,10]. The limited availability of O_2 molecules in the air (21 %) and the accumulation of water, a byproduct of the cathodic reaction, impede mass transport through the cathode catalyst layer pore network. Hence the pore network structure along with the catalyst material itself plays a crucial role in fuel cell performance [11–13]. A well-connected pore network in the catalyst layer ensures effective mass transport and maximizes the exposure of catalyst active sites [14,15].

Several factors, such as dispersion recipe and production process parameters, significantly influence the microstructure of the catalyst layer. Numerous studies have focused on manipulating the catalyst layer microstructure to achieve better fuel cell performance [16–21]. Fine-tuning the catalyst layer microstructure has been accomplished through various methods, including changing solvents in the catalyst dispersion recipe, altering catalyst particle shapes and sizes, modifying coating parameters, and adjusting drying temperatures. Woo et al. studied the effect of varying the solvent composition on the dispersion stability, rheological properties and cracking behavior in the catalyst layer by changing the content of water and 1-propanol in the dispersion [22]. Zhang et al. investigated the effect of solvent mixture with different alcohols, namely n-propanol, isopropanol, ethanol, and methanol, on the construction of the catalyst layer network and its resulting electrochemical performance [22]. Yim et al. fabricated a distinct cathode catalyst layer microstructure by changing decal process parameters and studied its effect on the final electrochemical performance of the PEMFC [22].

In the above-mentioned studies, the catalyst layers were primarily analyzed for their physical properties using imaging techniques such as SEM, AFM, and optical profilometry. Two of the most employed methods for assessing pore characteristics in catalyst layers are Mercury and nitrogen physisorption. Beyond this, several studies have shifted focus towards synchrotron X-ray imaging to perform operando analyses on various fuel cell components,

including catalyst layers, microporous layers (MPL), and gas diffusion layers (GDL) [23–26]. Markötter et al. utilized through-plane synchrotron operando imaging to investigate the influence of micrometer-sized MPL cracks on water transport dynamics properties [24]. Additionally, J. Liu et al. employed operando synchrotron X-ray computed tomography to explore the impact of different interfaces—specifically, the catalyst layer-membrane interface in CCM configurations, the catalyst layer-GDL interface in gas diffusion electrode configurations, and a hybrid CCM-GDE configuration—on fuel cell performance using platinum group metal-free electrodes [26].

However, despite significant advancements in techniques for analyzing the microstructural properties of catalyst layers—many of which now offer substantial information for comparative studies—these methods remain limited to quantitatively assessing properties such as surface roughness, inhomogeneity, pore size distribution, and porosity. While these techniques provide a useful qualitative overview of the catalyst layer's microstructure, they fall short in delivering detailed and quantitative insights into the pore network and geometry, which are essential for optimizing the pore structure for enhanced performance. For achieving knowledge-based design, there remains a need for fast, simple, and cost-effective techniques that can offer accurate and detailed pore network information.

To close this knowledge-gap, in this study, we developed a multi-scale approach for the structural analysis of catalyst layers that enables to characterize the quality of catalyst layers in terms of their morphology and microstructural properties. This method integrates MIP, microscopic imaging techniques, and digital image processing of cross-section images of catalyst layers. It is to be understood as a multiscale zoom-in approach, systematically utilizing different devices to capture the physical features of the catalyst layer across various size regimes. Finally, an in-house image analysis algorithm, for processing FIB-SEM cross-section images, developed in MATLAB enables a detailed, quantitative examination of pore geometry, porosity, and pore size variations across catalyst layers. Altogether, this approach, illustrated in a schematic diagram in Supplementary Figure S1, provides both qualitative and quantitative insights into the pore structure and sizes ranging from 10 nm to 10 µm.

For validation, as a direct application-scenario, a systematic design of experiments (DOE) was implemented to investigate the effects of different cathode catalyst dispersion compositions (by altering the proportions of alcohol, water, and ionomer) and varying hot-pressing forces on the morphological and microstructural properties of the catalyst layer, utilizing the developed multi-scale catalyst analysis method. The structural analysis data acquired was then utilized to explain the observed differences in fuel cell performance characteristics across the produced catalyst layers. Our method revealed structural nuances

previously hidden within imaging data, offering a deeper understanding of catalyst layer microstructure and its influence on performance. Although the image analysis is limited to a 2D representation of pores, it offers a cost-effective and fast alternative to complementary nano-computed tomography (nano-CT) for 3D pore imaging at voxel resolutions below 10 nm.

2. Experimental section

2.1 Preparation of CCMs

Indirect coating of membranes, also known as the decal transfer approach, was followed for the preparation of catalyst coated membranes [27]. In brief, the cathode catalyst dispersion is composed of the commercially available carbon-black-supported Pt catalyst powder (50 wt.% Pt), a binder (solution of perfluoro sulfonic acid with a perfluorinated backbone), and 1-propanol and water as solvents. The mixture was dispersed using a high shear rotary dispersion device (Kinematica Polytron) for 10 minutes. The ionomer to catalyst (I/C) ratio and alcohol to water (A/W) ratio were varied for different dispersions keeping the solid content constant. The first dispersion (dispA) contains a high I/C ratio and high A/W ratio while the second one (dispB) contains a low I/C ratio and high A/W ratio. Both I/C ratio and A/W ratio were kept low for the third dispersion (dispC). Due to data confidentiality agreements a more detailed information about the dispersion recipe cannot be provided.

The prepared dispersions were coated onto a decal film using a tabletop doctor blade (TQC Sheen) at a coating speed of 20 mm/s and a wet layer thickness of 150 µm. This was done on a vacuum bed heated to 50 ºC. For the preparation of half-CCMs, the catalyst-coated decal films were hot-pressed (LaboPress P300 S, Vogt) with a commercially available perfluoro sulfonic acid (PFSA) membrane (15 µm thick) at 160 °C for 10 minutes over an area of 36 cm², using a PTFE film to protect the membrane's open side. Hot-pressing was conducted under a range of pressures from 0.23 MPa to 7.1 MPa. For full CCMs, the same parameters were applied, but the protective PTFE foil was replaced by an anode catalyst-coated decal film.

2.2 Microstructural characterization of catalyst layers

2.2.1 Microscopy of catalyst layers

The catalyst layers were analyzed using a carefully chosen set of microscopy techniques to study their surface properties. Optical profilometry (S Neox 090) was performed at 50X magnification. Atomic force microscopy (AFM, Anton Paar Tosca 400) in tapping mode was employed to examine the surface features over a 10 µm x 10 µm window. Additionally, scanning electron microscopy (SEM, Helios NanoLab 600i) was used to investigate finer surface details.

2.2.2 Mercury intrusion porosimetry

The catalyst layers were investigated for the pore size distribution of surface open pores using MIP (Anton Paar Porosimeter 60). Half-CCMs, measuring 3 cm x 6 cm, were sectioned into 1 cm x 1 cm pieces for the MIP analysis. The samples were weighed prior to the measurement to normalize the volume of intruded mercury relative to the sample mass. The measurement cell, containing the sample, was initially evacuated to 9.66 x 10^{-4} PSI before being filled with mercury. The applied pressure on the high-pressure unit of the device is set to increase from 20 PSI to 60,000 PSI during the measurement.

2.2.2 Cross-section imaging using focused ion beam–scanning electron microscope

The catalyst layers in the form of half-CCMs were cut into 0.5 cm x 0.5 cm pieces and mounted on the SEM sample holder using carbon tape. The commercial PFSA based membrane, which is electrically non-conductive, is sandwiched between the carbon tape and the catalyst layer. To ensure electrical conductivity between the catalyst layer and the sample holder, a few drops of silver glue were applied at the edges of the half-CCM, connecting both the catalyst layer and the carbon tape. A Helios NanoLab 600i SEM device equipped with a FIB was used to obtain cross-section images. Prior to the cross-section process, a protective platinum line (15 µm x 0.5 µm, 0.5 µm thick) was deposited using the platinum deposition system of the FIB-SEM to shield the underlying structure from high-energy FIBs.

A rectangular area (15 µm x 15 µm) was selected adjacent to the platinum line for creating a 15 µm deep hole using a 6.5 nA FIB beam current (Supplementary Figure S2). The undamaged wall beneath the platinum deposition was the focus for SEM imaging. This wall was polished using ion beams with lower current (up to 93 pA) to achieve a smooth cross-section. Using higher ion beam currents can expedite material removal; however, it often produces a rougher surface and can induce thermal reactions over larger areas, potentially causing particles deeper within the material to melt. In contrast, lower currents minimize these thermal effects, resulting in a smoother cross-sectional surface but at a slower removal rate. Optimizing between beam current, processing time, and associated costs is therefore essential, as each factor impacts the quality of the cross-section. Finally, images at multiple resolutions were captured by SEM.

2.2.3 Adhesion analysis

To determine the transferability of the catalyst layers from the release liner to the membrane, the centrifugal adhesion analyzer Lumifrac from the company LUM was used. The samples have been prepared as described in detail in the work of Grebener et al. [28]. Briefly, the hot-pressed samples were cut into specimens of 10 mm diameter without separating the membrane and catalyst from the decal film. With a double-sided adhesive tape (Lohmann Duplocoll 362.2), the membrane side was glued onto a rigid backplate and the decal film to an adapter which was bearing a copper test mass. In the centrifuge, the copper mass applied a centrifugal force that acted as a tensile stress to the membrane-catalyst layer-decal film system. A guiding sleeve ensured perpendicularity, and a detector determined the frequency at which the system breaks which is measured when the copper mass hits the detector. The success or failure of the transfer was realized by visual inspection as in the case of good transferability none of the black catalyst layer should remain on the surface of the decal film.

2.3 Electrochemical characterization

All the electrochemical tests on the catalyst layers in the form of full CCMs were performed using a single-cell setup (quickCONNECTfixture FC25) from balticFuelcells GmbH, with an MEA active surface area of 25 cm^2. The CCMs along with the gas diffusion layers (anode: Freudenberg H23C8, cathode: AvCarb MB30) were sandwiched between the gas flow field plates at a clamping pressure of 3.5 bar(g). The cell temperature was maintained at 80 ^oC, and the relative humidity of H_2 gas and air at 80 %. Polarization curves were recorded under two different stoichiometric coefficients (λ) for anode and cathode, set at 2 and 5, respectively. The stoichiometric coefficients represent the multiples of the mass flow rates of H_2 and O_2 in air relative to the minimum theoretically calculated amounts, as per Faraday's law, required for complete reactant utilization. Thus, stoichiometric coefficient 1 ensures zero reactant concentration at the PEMFC outlets, i.e. complete reactant utilization at the given current density at each measuring point of the polarization curve. For instance, a stoichiometric coefficient of 2 indicates that the mass flow rates of H_2 and air are twice as high as the minimum theoretical requirement for the reaction. Higher stoichiometric coefficients enhance the delivery of reactant gases to the catalyst and improve water management by efficiently discharging produced water and vapor from the cathode, ensuring optimal performance and preventing pore occlusion over time. Both measurements were performed at 2.5 bar(abs).

The humidified gases were provided by a test bench built by MS2 company. This also contains the electrical load (Höcherl & Hackerl PLI1206ZVSV6SA6), the device for measuring the high-frequency resistance (Schütz Ohmmeter MR2212W) and the device for evaluating the electrochemical impedance spectroscopy (EIS) measurement data (Gamry Interface 5000

E). All test bench components such as the mass flow controller, humidifier, electrical load and electrochemical measuring devices are controlled by the MS2 software and by specially adapted test protocols. These enable the automatic execution of consecutive test-phases like leakage tests, CCM-conditioning, polarization curves, EIS data recording, cyclic voltammetry and hydrogen-crossover measurements.

3. Results and Discussion

The study focuses on the development of a robust method for multi-scale catalyst layer characterization that integrates MIP, FIB-SEM, and conventional microscopy techniques. Through the application of a custom-developed MATLAB-based image analysis algorithm, quantitative parameters such as pore size, porosity, and geometry were systematically extracted from the FIB-SEM images. This methodology was then applied to investigate the influence of process parameters and dispersion properties on the microstructural characteristics of CCMs in PEMFCs.

To achieve this, catalyst layers were fabricated using three distinct dispersions with varying I/C and A/W ratios, specifically selected to examine the effects of dispersion composition on microstructural attributes. These CCMs, exhibiting unique microstructural characteristics, were subjected to a range of pressures during the decal transfer process to elucidate the impact of hot-pressing pressure on structural properties. Further, to evaluate the implications of these microstructural modifications on the usability and performance of CCMs, adhesion and transferability analysis were conducted, followed by a series of electrochemical tests. By correlating the microstructural features with performance metrics, our study enabled us to establish a set of robust process parameter-microstructural property-performance relationships.

3.1 Catalyst layer characteristics

3.1.1 Pore characteristics and assignments

MIP has traditionally been used to analyze open pores in various materials. Mercury, being a non-wetting liquid, intrudes into pores only under external pressure. According to the Washburn equation (Equation 1), assuming the pores are cylindrical in shape, there is an inverse relationship between the pore opening diameter and the applied pressure [29,30]. This equation enables the generation of pore size distribution curves from standard mercury volume intrusion profiles, such as those shown in Figure 1. MIP measurements were not only performed on the catalyst layers but also performed on the PFSA-based membrane to assess its effect on CCM porosity measurements. The membrane used in the CCM preparation has no pores that in the region of our interest (10 nm to 20 µm) can be assessed by MIP

(Supplementary Figure S3), which is consistent with previous reports in the literature [19,31]. Thus, all Hg intrusions in the CCMs are solely due to the catalyst layer, with no contribution from the membrane.

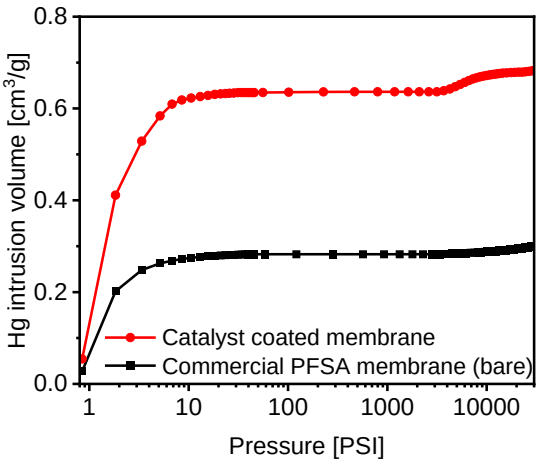

Figure 1: Mercury intrusion volume profiles of half CCMs and uncoated PFSA-based membranes.

The pore size distribution of a typical half-CCM is characterized by two distinct regions. The first region corresponds to the low-pressure range (1 PSI to 7 PSI), representing large-pore diameters, as illustrated in Figure 2a. A notable feature in this region is a peak around 20 μm, associated with larger pores. However, this peak is often poorly resolved due to material compression during the initial phase of mercury intrusion, which causes interference and overlaps with device readings. Consequently, the larger pore peak frequently appears as a shoulder rather than a distinct feature, requiring cautious interpretation of pore sizes in this range to account for potential compression-induced artifacts. The second region, corresponding to high pressures (3000 PSI to 8000 PSI), represents small-pore diameters, as depicted in Figure 2d. This region is characterized by a distinct peak corresponding to pores in the range of 10 nm to 100 nm, likely formed between catalyst particles.

Further insights into the origin of the two characteristic pore features can be gained by cross-referencing the MIP data with microscope images, allowing for a more comprehensive understanding of the underlying pore structure. In Figure 2b, images gained by optical profilometry that can assess characteristics in the size range of 10 μm to a few hundreds of microns, cracks of tens of microns in size are clearly visible on the surface of the CCM. Also, when one such crack is located and magnified using AFM, the depth of it was found to be around 2 microns. From the combination of optical profilometer data and AFM images, it can be concluded that the shoulder peak observed around 20 μm in the pore size distribution can be ascribed to the cracks present on the surface of the catalyst layer. The second peak, between 10 nm and 100 nm, is due to the intraparticle or secondary pores in the catalyst layer

[31,32]. This is further confirmed by closer inspection with AFM and FIB-SEM (Figure 2e, 2f), where secondary pores matching the respective peak in the pore size distribution are clearly visible.

Thus, we have successfully decoded and assigned all key features in the MIP pore size distribution to corresponding microstructural characteristics of the CCMs, as observed through various microscopy techniques. This comprehensive understanding allows us to confidently use the herein proposed *MIP-microscopy correlative method* as a tool for analyzing microstructural changes that occur as production parameters, such as catalyst dispersion composition and hot-pressing force, are varied.

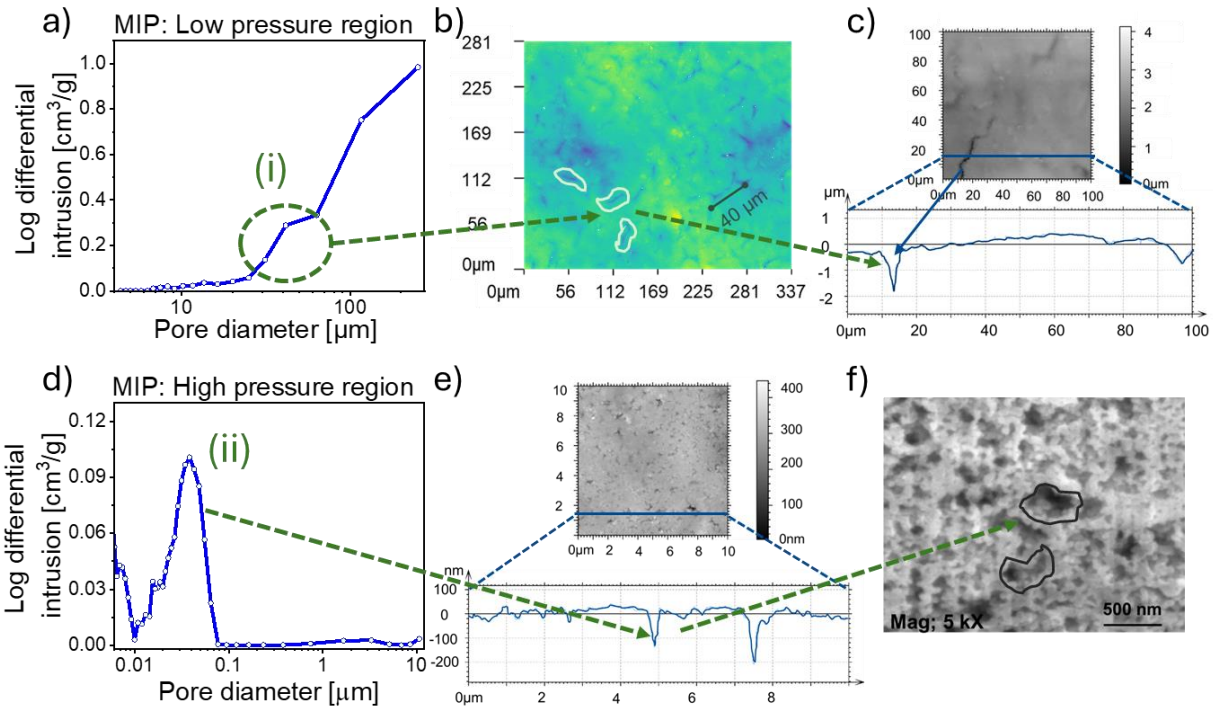

Figure 2: Identifying features in the MIP pore size distribution using AFM, optical profilometry, and SEM. (a), (b), and (c) show the MIP peak, optical profilometer image, and AFM image of cracks on the catalyst layer surface, respectively; (d), (e), and (f) display the secondary pores in the catalyst layers, as recorded by MIP, AFM and SEM, respectively.

3.1.2 Effect of dispersion formulation on catalyst layer microstructure

In one of our previous studies, we demonstrated a DoE where variations in the formulation of catalyst layer dispersions lead to differences in flow properties, sedimentation behavior and the drying process. We found that even when the solid content and the dispersion processing parameters were kept constant, these differences ultimately impacted the microstructure of the CCM and its electrochemical performance [28]. In this work, the same DoE was carried out to generate catalyst layers coated on decal film with varying microstructure. By applying

the herein-developed microstructure assessment by means of the MIP-microscopy correlative method, we aim to get an even deeper understanding of the correlation between cathode catalyst layer dispersion formulation and processing, and the resulting microstructure of the cathode catalyst layer in CCMs.

As in our previous work, we selected three distinct dispersion formulations: dispA (high I/C and high A/W ratios), dispB (low I/C and high A/W ratio), and dispC (low I/C and low A/W ratios) [28]. Half-CCMs fabricated from these dispersions were analyzed using MIP, AFM and SEM. The pore size distributions obtained from MIP are presented in Figure 3a, which reveals clear differences in pore properties across catalyst layers originating from the three different dispersions. The secondary pores in the catalyst layers formed from dispA and dispB exhibited average pore sizes of 60 nm and 65 nm, with full width at half maximums (FWHM) of 34 nm and 44 nm, respectively. In contrast, the secondary pores in catalyst layers from dispC were smaller and centered at 40 nm, with a narrower distribution (FWHM of 16 nm). Additionally, the peak corresponding to surface cracks (centered at 3 µm) is notably more intense for half-CCMs made from dispC compared to those made from dispA and dispB. These findings are further corroborated by AFM images (Figure 3b-3c) and SEM data (Figure 3e-3g), which show significantly more cracks and pinhole defects in the catalyst layer from dispC than in those from dispA and dispB.

In line with the findings from our previous work, the observed differences in microstructure can be attributed to the chemical composition of each of the dispersions. For dispA and dispB, with a high A/W ratio, the mixture exceeds the azeotropic point, causing preferential evaporation of water during drying, which prevents its accumulation in the catalyst layer. In contrast, dispC, with a low A/W ratio, allows water to accumulate as it is depleted from 1-propanol. As water remains in low-temperature spots for longer periods, it appears to migrate within the coating, forming wet spots of varying sizes. The slow evaporation from these spots promotes crack formation over time [22,33,34]. As these cracks form in the drying process of dispC, the catalyst particles move closer together due to the increased cohesion caused by the higher capillary forces generated by water at the wet spots. This closer packing of particles reduces the secondary porosity, explaining the smaller average secondary pore size observed in catalyst layers produced from dispC, compared to those from dispA and dispB. At this point, it is important to mention that a trace amount of residual water content may remain in the catalyst layers even after drying at 50°C. This residual could then gradually evaporate during the interval between drying and hot-pressing. However, there was no water condensation observed on the decal foil after the hot-pressing. This indicates that any residual water in the catalyst layer is insufficient to cause significant microstructural changes. Consequently, the observed microstructural modifications during hot-pressing are primarily attributed to the

softening of polymers due to the elevated temperature and the mechanical stress applied. A more detailed investigation into the microprocesses during the drying stage will be explored in future studies.

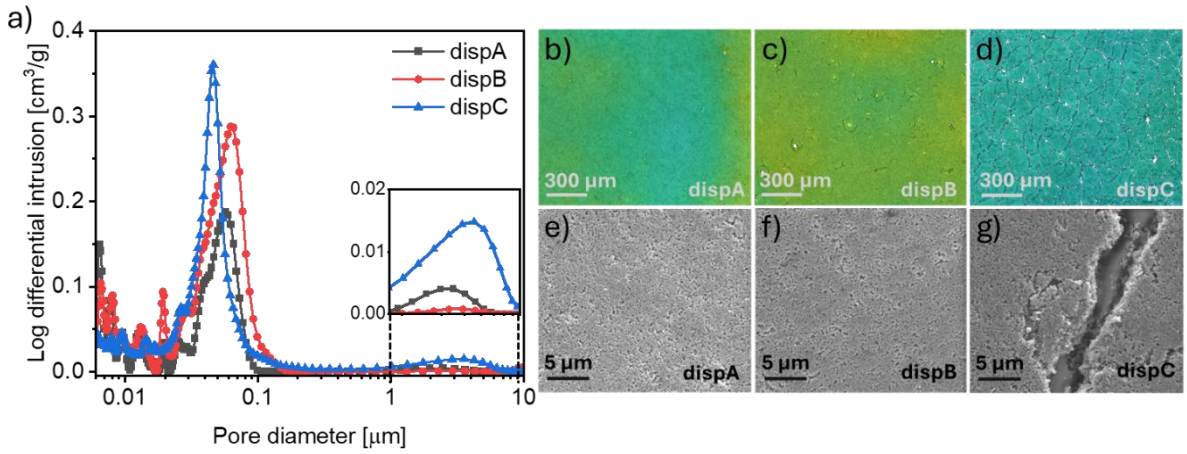

Figure 3: Comparison of cathode catalyst layers, after decal transfer, fabricated from different dispersions. Panel (a) shows the pore size distribution, acquired from Hg-intrusion porosimeter, for different catalyst layers; panels (b), (c) and (d) show the optical profilometer images of the surface of the catalyst layers; panels (e), (f), and (g) show the SEM images of the surface of the catalyst layers.

So far, our findings demonstrate that the formulation of catalyst layer dispersions plays a critical role in shaping the microstructure of catalyst layers in CCMs, which can in turn affect their electrochemical performance. Through MIP-microscopy correlative analysis method, we were able to correlate the pore size distribution with surface-level microstructural features, providing valuable insights into surface cracks and surface open pores. However, this method is inherently limited to surface characteristics. To obtain a more comprehensive understanding of the bulk pore distribution, coverage, and geometry within the catalyst layer, advanced techniques like FIB-SEM are necessary. FIB-SEM, when combined with computational image processing, allows for detailed visualization of the internal pore network, offering essential insights for optimizing catalyst layer formulations and their subsequent processing. For this analysis, we selected CCMs with two distinct surface morphologies—dispA and dispC—and utilized FIB-SEM to capture cross-sectional images, enabling a deeper investigation of their internal structures.

3.1.3 FIB-SEM and image analysis

Image pre-processing.

Traditionally, FIB-SEM cross-sectional images have been used to qualitatively compare catalyst layers in terms of pore sizes, porosity, and height differences [35,36]. Although FIB-SEM images contain extensive quantitative information, they are rarely used for this purpose. To extract this valuable information, an image processing algorithm was developed in MATLAB. Figure 4 illustrates the steps in the developed image processing algorithm for converting the raw FIB-SEM image into a calculable logical matrix. Initially, the raw images from FIB-SEM, in formats like JPEG or PNG, are loaded into the program. These images are then preprocessed using median filtering (medfilt2 in MATLAB) to reduce graininess and enhance the contrast between catalyst particles (foreground) and pores (background), as shown in Figure 4b. This preprocessing step helps mitigate noise and artifacts from the FIB-SEM device. Further, the preprocessed images are binarized, with black pixels corresponding to catalyst particles and white pixels representing pores (Figure 4c). The final binarized images, essentially logical matrices of 1's and 0's (Figure 4d), provide a format suitable for detailed mathematical calculations of pore properties. The calculations are explained in the following section.

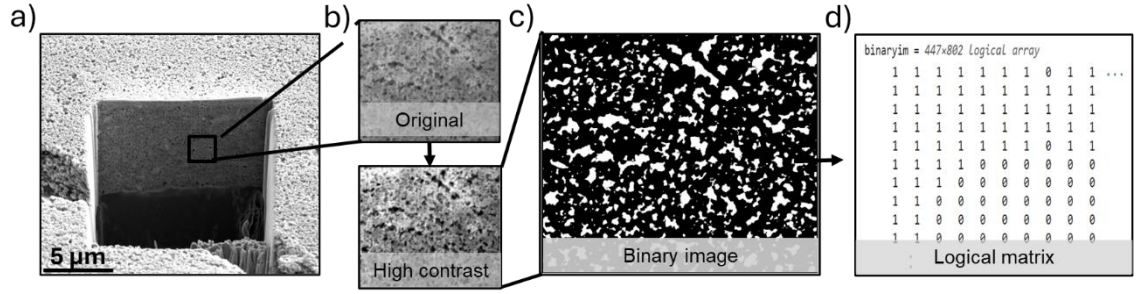

Figure 4: Steps in the image processing algorithm developed in MATLAB. (a) FIB-SEM cross-sectional image of the catalyst layer; (b) pre-processing of the raw FIB-SEM image to enhance foreground-background contrast; (c) binarized image representing pores and particles; (d) image converted into a logical matrix of 1's and 0's.

Pore size and geometry calculations from pre-processed images.

One of the essential microstructural properties of catalyst layers is pore coverage, indicating the proportion of space occupied by pores relative to catalyst particles. This metric can be derived from the logical matrix by calculating the ratio of entries representing catalyst particles (denoted as 0's) to the total entries within the matrix. Additionally, MATLAB's 'regionprops' function was employed to identify, segment, and assign unique identifiers to each connected pore. This segmentation allows for the measurement of individual pore sizes and

geometries within a two-dimensional frame. Pore size determination is performed by calculating the area of each connected pore and deriving the diameter of an equivalent circle.

Another key achievement of FIB-SEM image analysis is the capability to obtain detailed information about the geometry of pore cross-sections. The pore geometry was analyzed using a metric known as circularity, which quantifies how closely the shape of a pore cross-section resembles a perfect circle. Circularity is calculated as:

$$Circularity = \frac{4 \times \pi \times Area}{Perimeter^2} \qquad \text{(Equation 1)}$$

A perfectly circular pore cross-section has a circularity value of 1, the highest possible value, as a circle represents the minimum perimeter for a given area. This property implies that circular pores expose the least amount of catalyst surface relative to their size, thereby limiting active catalyst exposure for electrochemical reactions. In this context, we expect non-circular pore shapes being advantageous, as they provide a larger perimeter for catalyst particle exposure per unit area. Thus, a circularity value deviating from 1 is beneficial, promoting a more effective catalyst layer structure for electrochemical performance.

The herein developed image processing algorithm was applied to generate a detailed pore size distribution (Figure 5c) for catalyst layers with distinct microstructural characteristics, such as surface cracks and pore sizes, previously identified in the MIP-microscopy correlative study. As described above, catalyst layers were produced from dispA and dispC under consistent processing conditions. A key observation from this distribution is that catalyst layers from dispA contain larger pores than those from dispC. The average pore size for the catalyst layer obtained from dispA is 148 nm while that for the catalyst layer obtained from dispC is 113 nm. This trend is visually apparent from the binarized cross-section images of the respective catalyst layers, and the underlying factors contributing to these differences are discussed in Section 3.1.2.

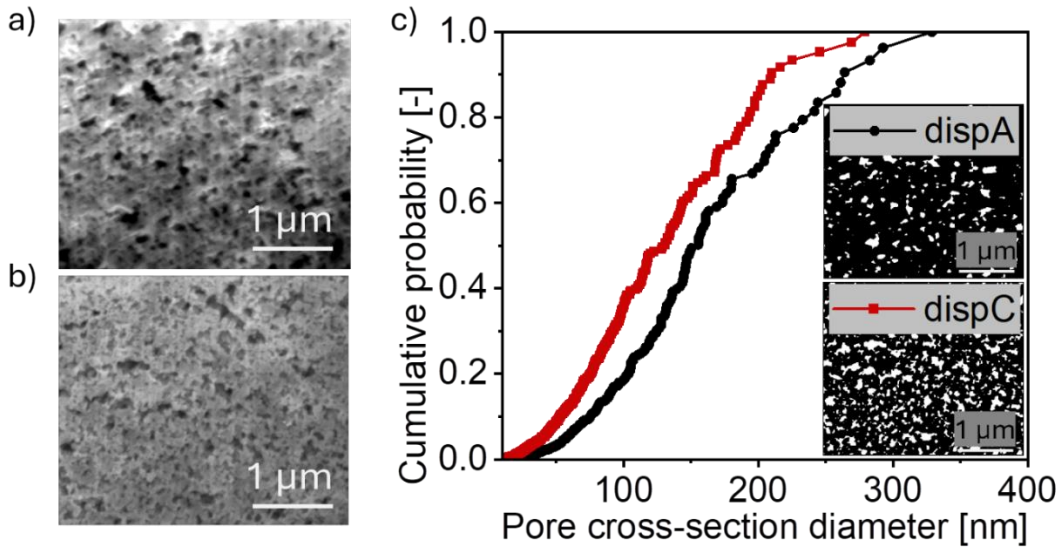

Figure 5: Pore size distribution of catalyst layers, derived from image analysis of FIB-SEM data. Cross-section images of cathode catalyst layers, after decal process, prepared from (a) dispA and (b) dispC; (c) pore cross-section diameter distribution.

Taken together, the pore size distributions derived from both FIB-SEM image analysis and MIP exhibit a consistent trend across the dispersions. However, there is a notable discrepancy between the pore size distributions derived from FIB-SEM image analysis and those obtained via MIP. For almost all samples, the average pore size estimated via MIP is approximately 70 nm to 80 nm smaller than that derived from FIB-SEM image analysis for the same samples. This disparity arises primarily from differences in the underlying assumptions used in estimating pore sizes. In MIP, pores are assumed to be cylindrical, with the pore size being defined by the cylinder's diameter. For ink-bottle-shaped pores, which feature a narrow pore opening leading to a larger cavity, MIP estimates the pore size based on the diameter of the opening as this caused the largest pressure. Hence, the assumption of cylindrical pores can lead to inaccuracies, as it does not account for the actual pore geometry. Additionally, the high external pressures applied during MIP measurements can cause some pores to collapse before mercury intrusion, further leading to an underestimation of pore sizes [29,30]. Consequently, and the community needs to be aware of that, the pore size measurements from MIP tend to be smaller than those obtained from FIB-SEM cross-sectional image analysis of the same sample.

So far, we introduced a novel approach by employing a correlative MIP-microscopy technique to comprehensively characterize catalyst layer microstructures, allowing for a more thorough understanding of pore distributions and surface morphologies. The newly developed image processing algorithm enhances this approach, enabling quantitative analysis of FIB-SEM images by extracting detailed information on pore coverage, size, and geometry directly

from cross-sectional data. Traditional pore analysis techniques, such as MIP, do not effectively provide this level of detail, but of course, can be executed at a significantly higher throughput. At this point it also needs to be mentioned that nano-computed tomography (nano-CT) is one of the excellent techniques for obtaining detailed 3D microstructural insights for gas diffusion layers. But achieving voxel resolutions below 10 nm with nano-CT is both costly and time-consuming, especially when high sample throughput is needed. In contrast, FIB-SEM image analysis, while limited to a 2D representation of pores, provides a more efficient and cost-effective solution for studies requiring high-throughput analysis or comparative evaluations across multiple samples from the same or different electrode batches. This methodology provided essential insights into the distinct microstructural differences in catalyst layers derived from various dispersions, linking specific dispersion formulations to variations in pore size and surface features. Such insights not only clarify the underlying causes of microstructural variations observed across dispersions but also offer valuable guidance for optimizing dispersion formulations to improve electrochemical performance in fuel cell catalyst layers.

3.2 Influence of hot-press pressure

Building on our analysis of dispersion formulation, we further investigated the impact of the hot-pressing pressure as an additional processing parameter that governs the microstructure of the catalyst layers within a CCM. CCMs with an area of 42.25 cm² were fabricated from the three model dispersions (dispA, dispB, and dispC) and hot-pressed at pressures of 1.18 MPa, 2.37 MPa, 3.55 MPa, 4.73 MPa, achieved by applying forces of 5 kN, 10 kN, 15 kN, 20 kN respectively. This process was conducted at a temperature of 160 °C, which exceeds the glass transition temperatures of PFSA polymers like Nafion (125 C) and Aquivion (145 C) that are frequently used in the field of PEMFC. Figure 6 presents the MIP measurements for catalyst layers prepared using these parameters. These measurements reveal that the direction and rate of porosity change in response to the hot-pressing pressure depend on the dispersion formulation of the catalyst layers. For catalyst layers derived from dispA and dispB, there is a clear decrease in porosity as the hot-pressing pressure increases (Figures 6a and 6b). This trend reflects a densification effect within the catalyst layer under higher pressures. The observed reduction in porosity can be attributed to the softening of the PFAS polymers above the glass transition temperature during the hot-pressing, which allows catalyst particles to pack more densely under applied pressure. Upon cooling, this process induces plastic deformation in the CCMs, resulting in a lasting decrease in the pore volume within the catalyst layers [20,36,37].

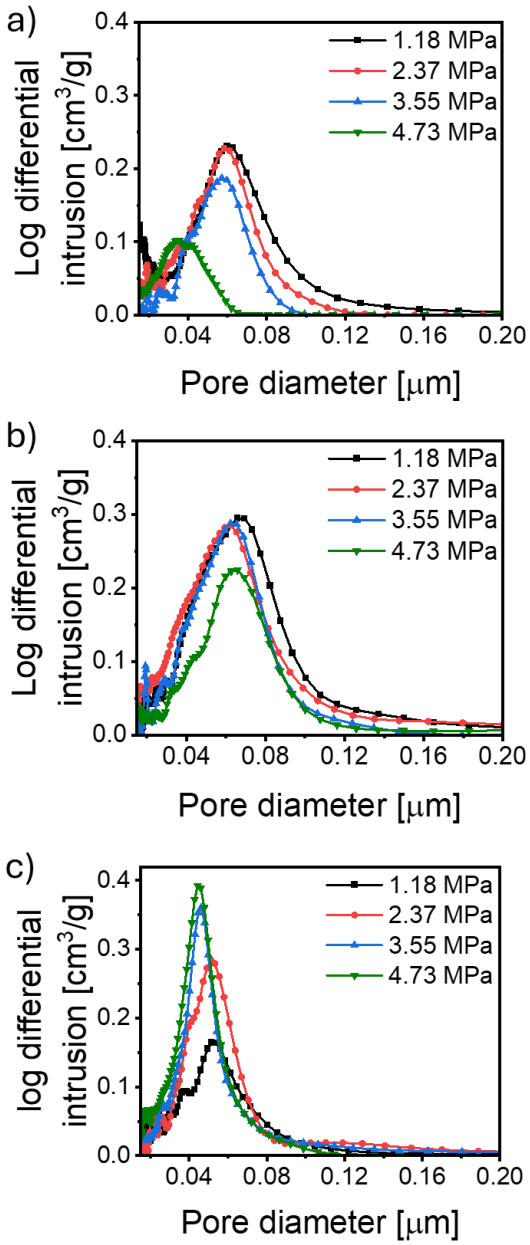

Figure 6: MIP pore size distribution of CCMs from a) dispA b) dispB and c) dispC, prepared under a hot-press area of 42.25 cm^2 at 160 °C.

In contrast to expectations and observations with other dispersions, catalyst layers derived from dispC exhibit an increase in their overall porosity with rising hot-pressing pressure (Figure 6c). Notably, despite the increase in the overall porosity, a negative shift in the peak position from 52 nm to 44 nm occurs as the hot-pressing pressure rises from 1.18 MPa to 4.73 MPa, indicating a reduction in the average pore size with increasing pressure. While this reduction in average pore size aligns with typical expectations due to the compaction of pores under pressure, the simultaneous increase in the overall porosity with rising pressure is an unusual and unexpected observation.

This phenomenon can be attributed to the distinct chemical composition of each dispersion. In a prior observation (Section 3.1.2), the analysis of pore structures across different dispersions revealed that the average secondary pore size in catalyst layers derived from dispC is smaller than that observed in those made from dispA and dispB. This difference is due to the higher water content in dispC, which delays water evaporation and leads to the formation of wet patches on the catalyst layer surface. As a result, particles within these patches come closer, forming aggregate structures under the influence of capillary forces exerted by the residual water. In contrast, catalyst layers derived from dispA and dispB experience more uniform and rapid drying due to their higher A/W ratios. This accelerated drying prevents particle aggregation and the formation of wetted patches, resulting in a more uniform pore structure with minimal cracking. Under hot-pressing, when the ionomer softens due to the increased temperature, those aggregates within the dispC catalyst layers may break down under the applied pressure, exposing previously inaccessible secondary pores. This process increases the availability of open pores, which subsequently raises the overall porosity as more pores become accessible to mercury intrusion. Thus, the increase in porosity with higher hot-press pressures observed in catalyst layers derived from dispC can be attributed to this breakdown of particle aggregates and the resultant accessibility of additional secondary pores.

For a more in-depth understanding of the microstructural changes occurring during hot-pressing, CCMs from dispA, processed under two distinct pressures (1.18 MPa and 4.73 MPa), were analyzed using FIB-SEM imaging. The results are shown in Figure 7. Preliminary cross-sectional image analysis revealed a change in catalyst layer thickness, despite both layers being prepared from the same dispersion and using the same doctor blade gap of 150 µm. The catalyst layer prepared at 1.18 MPa exhibits a thickness of 6.45 ± 0.20 µm (Figure 7a), while the layer prepared at 4.73 MPa has a reduced thickness of 5.40 ± 0.31 µm (Figure 7b). This observed decrease in thickness with increasing hot-pressing pressure aligns with the expected densification effect, whereby higher pressures facilitate closer particle packing, reducing the overall layer thickness.

In the binarized cross-section images presented in Figure 7a and Figure 7b, a notable difference in pore geometry between samples processed under 1.18 MPa and 4.73 MPa hot-press pressures is evident. The pores within the 4.73 MPa sample appear more rounded, whereas those in the 1.18 MPa sample exhibit greater irregularity and branching. This qualitative observation was further validated through quantitative analysis of pore circularity, depicted in Figure 7c. Circularity measurements reveal that pores in the 4.73 MPa catalyst layers have an average circularity value of 0.67, indicating a more rounded shape, while pores in the 1.18 MPa catalyst layers have a lower average circularity value of 0.48, reflecting their

irregular, branched structure. This indicates that at higher hot-press forces, when the particles are compacted and pores are compressed, the small branches and irregularities of the pores collapse, resulting in increased circularity.

Additionally, as shown in Figure 7d, pore size distribution analysis based on FIB-SEM images reveals that the average pore size in catalyst layers hot-pressed at higher pressures is lower than in those processed at lower pressures. Specifically, the catalyst layer hot-pressed at 4.73 MPa exhibits an average pore size of 125 nm, while the layer hot-pressed at 1.18 MPa has a larger average pore size of 187 nm. This trend is consistent with expectations: higher hot-press pressures lead to closer particle packing within the catalyst layer, which consequently reduces the size of inter-particle gaps or secondary pores.

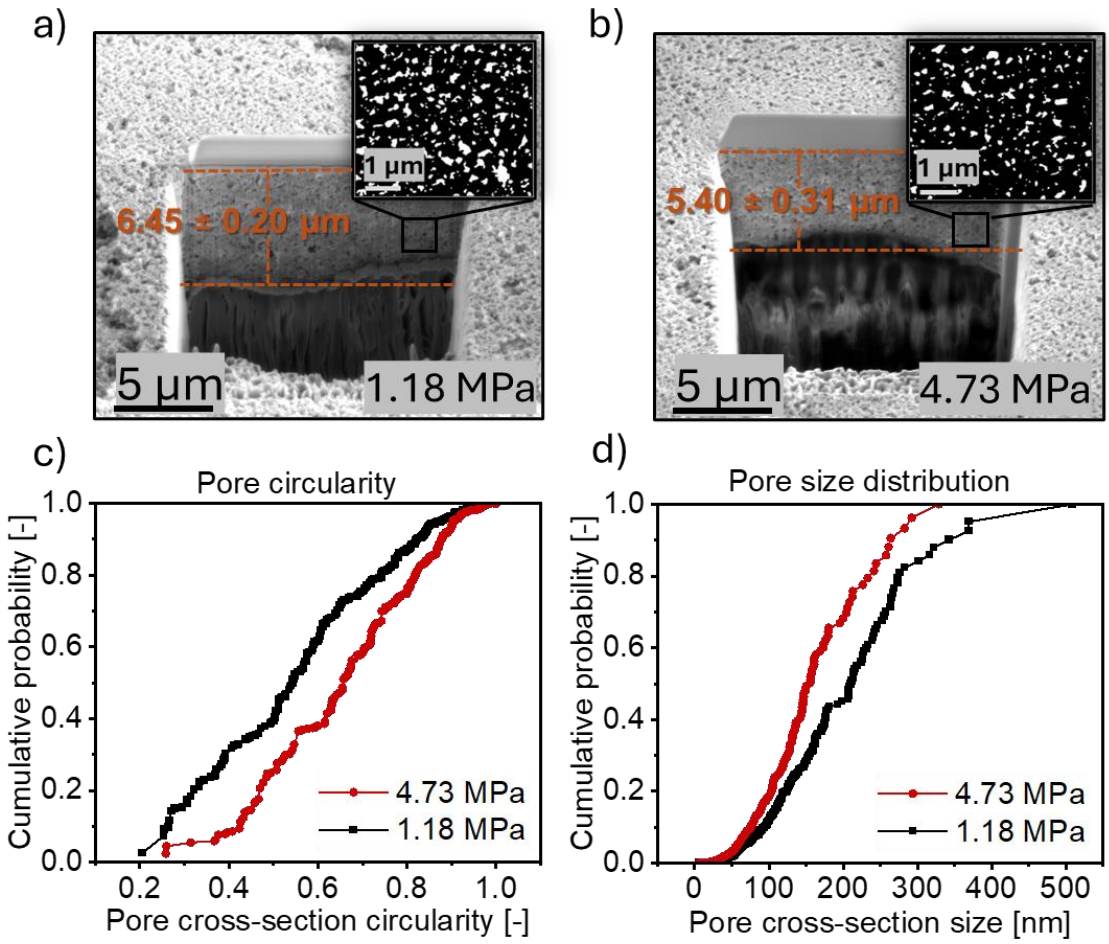

Figure 7: Comparative analysis using image processing on catalyst layer microstructure of CCMs prepared under different hot-pressing pressures. FIB-SEM cross-section images of CCMs hot-pressed at (a) 1.18 MPa and (b) 4.73 MPa; (c) pore cross-section circularity distribution; (d) pore cross-section size distribution.

In summary, this part of our study elucidates the intricate relationship between dispersion formulation and hot-pressing pressure with the microstructural properties of catalyst layers

within CCMs. By fabricating catalyst layers from three distinct dispersions and subjecting them to varying hot-pressing pressures, we uncovered significant differences in the porosity and pore network. Notably, the revelation that catalyst layers from different dispersions respond differently to hot-pressing conditions is a novel finding that strongly enhances our understanding of the catalyst layer microstructure. While catalyst layers from dispA and dispB exhibited a typical densification response characterized by reduced porosity with increased pressure, catalyst layers derived from dispC presented an unexpected increase in the overall porosity despite a decrease in the average pore size. This is attributed to the different drying mechanism that the catalyst layers undergo due to the different A/W ratio. Figure 8 presents a schematic diagram illustrating the proposed mechanisms.

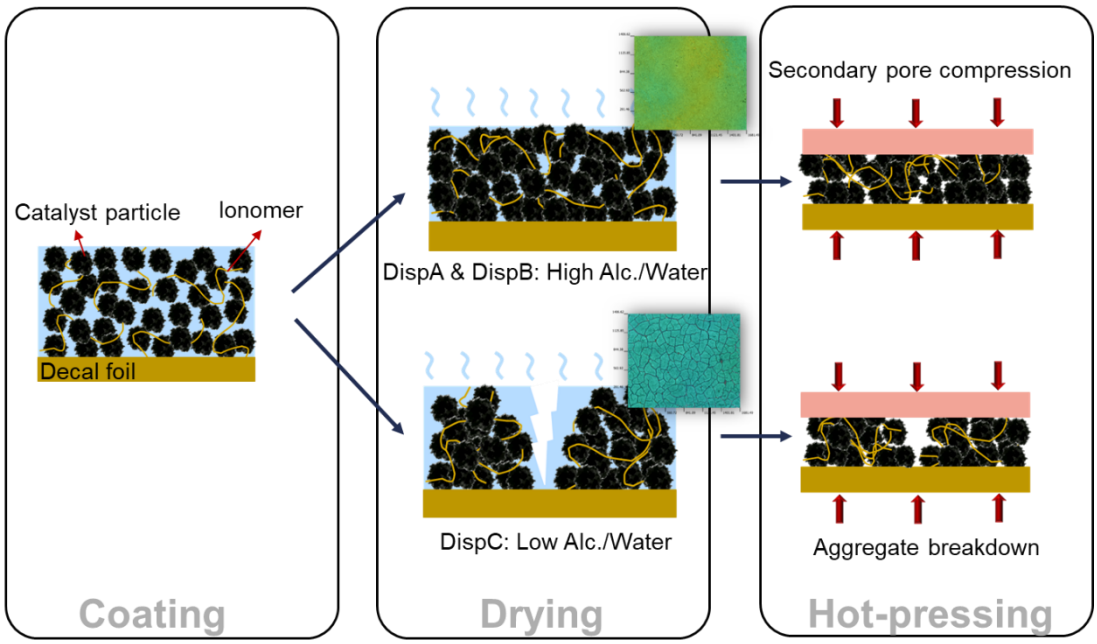

Figure 8: Schematic representation of structural changes that catalyst layers undergo during different stages of CCM fabrication.

Also, using FIB-SEM image analysis, we were able to reveal that during hot-pressing, it is not just the porosity and the mean pore sizes that change, but also the pore geometry undergoes significant alteration. These microstructural changes—such as alterations in porosity, pore sizes, and pore geometry—can directly impact catalyst layer performance, influencing mass transport and catalyst active site exposure. This relationship warrants further exploration through comprehensive electrochemical tests, the results of which are discussed in subsequent sections. Collectively, these findings underscore the complex interplay between processing parameters and microstructural outcomes, providing valuable insights for rationally optimizing catalyst layer performance in fuel cell applications.

3.3 Microstructural effects on catalyst layer functionality

So far, we have developed a robust microstructural analysis method capable of detecting even subtle changes arising from adjustments in process parameters during catalyst layer fabrication. This approach has allowed us to identify both, significant structural variations at the micrometer scale, associated with changes in dispersion formulations, as well as more nuanced alterations in secondary pore size and geometry resulting from modifications in hot-pressing parameters. Moving forward, it is essential to investigate how these observed microstructural changes—both major and minor—impact the useability and performance of the catalyst layers.

In the CCM production process, the step following coating and drying is the decal transfer of the catalyst layer, where catalyst material is transferred from a decal film to the membrane. Efficient transfer during this step is essential, as it minimizes material loss and thereby helps to reduce production costs. To investigate this process, an adhesion analysis was conducted on all hot-pressed samples from the three dispersions to assess transfer efficiency. Additionally, studying the electrochemical performance of the “effectively transferred” catalyst layers is crucial for understanding how microstructural variations induced by different process parameters impact functional performance. This approach will enable us to correlate microstructural characteristics directly with the catalyst layer functionality, thus bridging process parameters to final catalyst layer performance.

3.3.1 Adhesion behavior of catalyst layers

The hot-pressed half CCMs in the form of the decal film-catalyst layer-PFSA membrane-sandwich were tested for adhesion by centrifugation as described in Section 2.2.3. It needs to be mentioned that the adhesion analysis in this study was conducted at room temperature, rather than at elevated temperatures as they are typically encountered in industrial settings where the decal is performed immediately after the hot-pressing. The adhesion behavior is expected to vary with temperature due to the thermoplastic nature of the ionomer, decal foil, and membrane materials. Specifically, the transfer efficiency is likely to improve at hot-pressing temperatures and deteriorate as the temperature decreases. However, since the experiments were performed under the worst-case scenario in terms of temperature, with a constant temperature applied across all samples, we believe that comparative observations and conclusions derived from this study remain significant and reliable.

The decal process as illustrated in the work of Grebener et al. includes a coating step of the catalyst dispersion on the decal film, where it is dried in place [28]. A subsequent step, where decal film and catalyst layer are hot-pressed with a membrane, yields the CCM. The decal film should afterwards ideally be removed with the least possible amount of black catalyst residues on it, while the catalyst should remain on the membrane. Thus, the

transferability can be determined just by visual observation. The results are presented in Figure 9. The numerical adherence values are shown in Figure 9a, and it becomes clear that a minimum of adherence occurs for each catalyst formulation around 1.18 or 2.37 MPa with mean values of ≤ 0.2 MPa. The photographic scans in Figure 9b show the success or failure of the catalyst layer transfer. The comparison of the results in Figure 9a and 9b indicate that the transfer is optimal if the adherence is minimal with 0.2 MPa indicating a boundary. To investigate this correlation, micrographs for the formulation dispA are displayed in Figure 9c-9e. Three different failure modes were found. If the pressure during hot pressing is too low at 1.18 MPa, adherence increases, and cohesive breaking occurs. The catalyst residues are left with a characteristic fragmented appeal. If the hot-press pressure is set too high, 3.55 MPa and above, again cohesive breaking is detected, but with round-shape appeal, devoid of large fragmentations. In between, 2.37 MPa, only minor residues of some 10’s of micrometers can be found under microscope, thus the transfer is complete in all practical terms. If the pressure is further increased to 5.92 MPa, broken residues of the decal film can be found on the catalyst layer on the membrane, as the layered system of the decal film itself is breaking.

These results indicate that the decal process by hot pressing or roll lamination is very sensitive to the pressure applied. If the hot-press pressure is too low, the catalyst layer is not compressed enough, so it cannot establish enough cohesion to be intact after separation. Likewise, if the hot-press pressure is too high, new fragmentation seems to occur within the catalyst layer during hot pressing. Only the right level in terms of a small corridor of pressures in between these two cases seems to be just enough to cure fractures by compression but not inducing new ones. For dispB and of dispC, the first breaking mechanic cannot be found, only the complete transfer at 2.37 MPa for B and 1.18 MPa for C and cohesive failure mode above these pressure levels with the distinct round shapes.

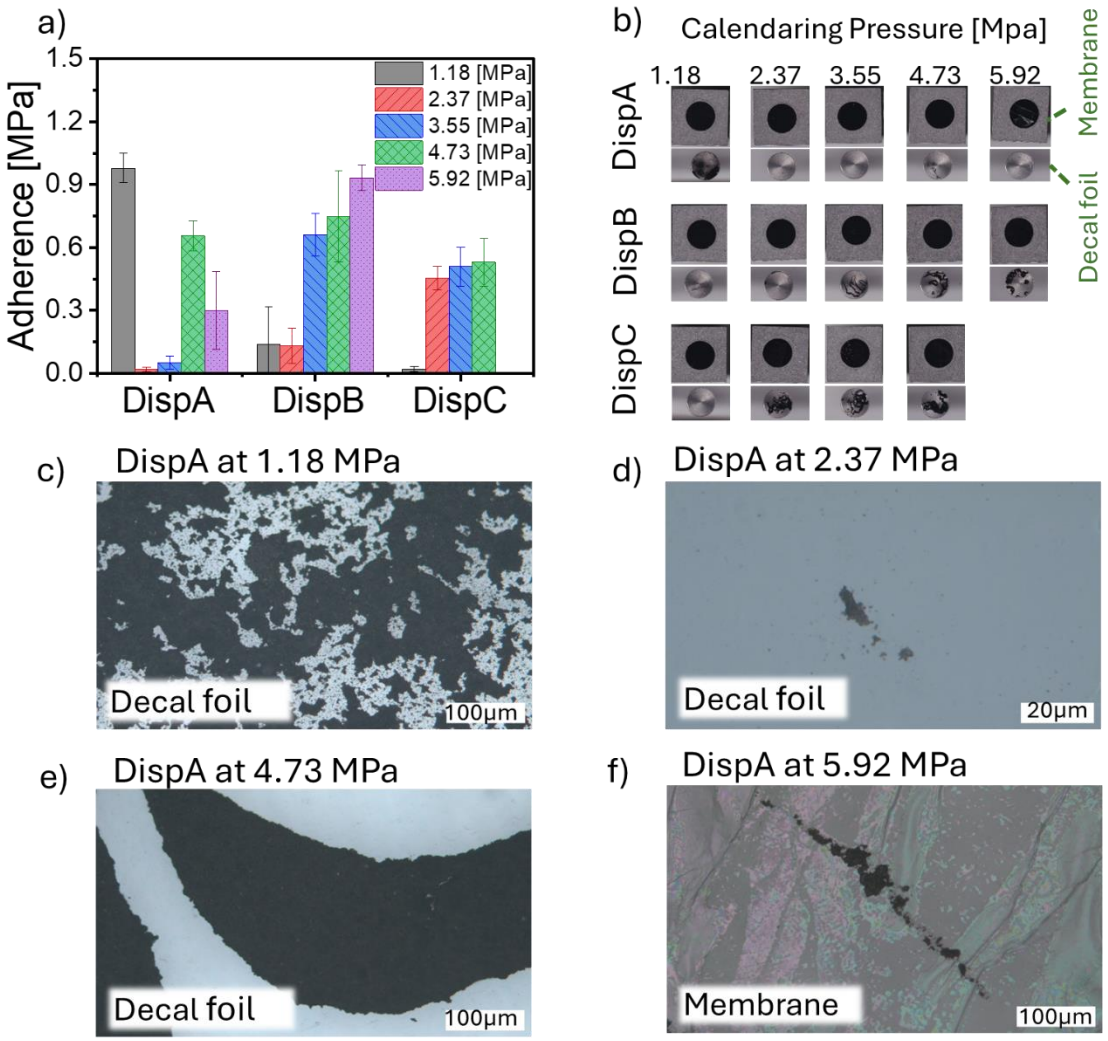

Figure 9: Adhesion and transferability of the catalyst layers from different catalyst dispersion formulations in dependence on the hot-pressing pressure. a) Adherence in numbers, displayed are mean and standard derivation; b) photographic scans of a representative specimen for each dispersion formulation and pressure. The membrane is on the top of each row with the steel backplate, the decal film is on the bottom with the 10 mm adapter. Transfer is to be complete, if none of the black catalyst material is left on the adapter; c)-f) micrographs of the decal film after hot-pressing at different pressure levels and transferring the catalyst layer in adhesion analysis experiment. Note, that in f) the release liner of the decal film itself breaks, creating interference colors.

3.3.2 Electrochemical performance of catalyst layers

In a prior study, we identified the impact of dispersion formulation on electrochemical performance, finding that catalyst layers produced from a formulation like dispA significantly outperformed those derived from dispB and dispC compositions [28]. This outcome persisted despite dispB catalyst layer exhibiting a microstructure seemingly better suited for mass transport and active site exposure. The superior performance of dispA catalyst layers can be attributed to their enhanced material transfer efficiency during the decal process, which led to

improved catalyst material availability. Additionally, the higher ionomer content in dispA catalyst layers promoted greater ionic conductivity, which further contributed to their enhanced performance [28]. In this study, we focus on the impact of the hot-pressing pressure on the electrochemical performance.

Hot-pressing can induce two major microstructural effects on the catalyst layer in CCMs:

1. During hot-pressing, the catalyst layer is compacted, reducing inter-particle spacing, also enhancing the contacts between the catalyst particles and the membrane. This effect was evident in the FIB-SEM cross-sectional images, where an increase in the hot-pressing pressure resulted in a measurable decrease in the thickness of the catalyst layer (Section 3.2). This closer packing may reduce the internal resistance of the CCMs, potentially enhancing the overall catalyst layer performance.
2. Compaction during hot-pressing also reduces the porosity and pore sizes within the catalyst layer, which can impact mass transport of reactants and product water throughout the layer. Additionally, changes in pore geometry, such as increased circularity and reduced branching, may limit the accessibility of active catalyst sites. This combination of reduced porosity and altered pore structure could, in turn, negatively affect catalyst layer performance. However, the significance of these microstructural changes on the electrochemical performance remains to be determined.

To investigate the impact of these structural changes, a series of electrochemical tests was conducted using a single-cell fuel cell setup. The catalyst layers analyzed were selected based on adhesion analysis, which demonstrated that only layers prepared from dispA achieved nearly 100 % material transfer across all tested hot-press pressures, making them the only viable samples for further performance evaluation.

Figure 10 represents the results of the electrochemical tests performed. EIS data shown in Figure 10a unravels that the ohmic resistance of the cell is reduced when the hot-pressing pressure increases. The ohmic resistance of CCMs prepared at hot-pressing pressures of 0.23 MPa, 1.18 MPa and 7.10 MPa was found to be 37.0 $m\Omega.cm^2$, 32.8 $m\Omega.cm^2$ and 29.7 $m\Omega.cm^2$ (EIS fitting at 2 A/cm^2) respectively. This trend in resistance is also observed in the high frequency resistance (HFR) curves shown in Figure 10b. These observations support our hypothesis that the hot-pressing pressure reduces the ohmic resistance of the fuel cell.

Fuel cell performance tests were conducted at two different stoichiometric coefficients to investigate the influence of the hot pressing on the different resistances and pore structure on CCM performance under varying mass transport conditions. As described in the experimental

part, high gas flow rates were set with an anode/cathode stoichiometric coefficient of 5/5, while low flow rates were set at a stoichiometric coefficient of 2/2. It has been reported that high gas flow rates at electrodes during the testing can alleviate mass transport losses associated with the secondary pore structure [19]. When high stoichiometric coefficient of reactant gases are used, the abundance of reactants mitigates the microstructural limitations. Also, the high airflow will help in the effective removal of product water from the cathode. In Figure 10c, the polarization curves at high stoichiometric coefficient of gases indicate a noticeable performance reduction in the high current density region starting at 2 A/cm^2 for CCMs prepared under lower hot-pressing pressures. The performance ranking is consistent with the predictions from the EIS analysis: CCM (1.18 MPa) ≥ CCM (7.10 MPa) >> CCM (0.23 MPa) at current density ≤ 3 A/cm^2. The differences in performance can be attributed to the contributions of ohmic resistance (Rohm), cathode charge transfer resistance (Rc), and diffusion resistance (Rdiff) (Figure 10d). While ohmic resistance decreases with increasing hot-pressing pressure, the cathode charge transfer resistance is lowest for the CCM hot-pressed at 1.18 MPa at current densities of 1, 2 and 3 A/cm^2 (Figure 10d, Supplementary Figure S4b, S4c). This can be due to the most optimal Pt/C distribution and the highest Pt utilization. Contrary to expectations, the lowest diffusion resistance is observed for the CCM hot-pressed at the highest pressure. This phenomenon can be attributed to the smaller pore sizes observed in CCMs hot-pressed at higher pressures, which accelerate airflow compared to the larger pores in CCMs hot-pressed at lower pressures during high gas flow measurements (Venturi effect). This enhanced airflow efficiency facilitates more effective removal of produced water, thereby improving water management in CCMs with smaller catalyst layer pores.

In general, the total resistance from the EIS spectra follows the trend of the cathode charge transfer resistance. This correlates with the best PEMFC performance for the CCM hot-pressed at 1.18 MPa and the lowest performance for the CCM hot-pressed at the lowest pressure, where the highest cathode charge transfer resistance has the most significant impact. Despite having the lowest ohmic and diffusion resistance, the CCM prepared at the highest hot-pressing pressure of 7.10 MPa, although very close in performance to the CCM prepared at the moderate pressure of 1.18 MPa, shows reduced PEMFC performance due to the higher cathode charge transfer resistance.

It is important to note that the resistance observed in the lower frequency region of the EIS spectra, where all resistances are summarized in the total resistance, is primarily responsible for the PEMFC performance. The performance trend predicted by the analysis of different resistances from EIS fitting is further confirmed by the capacitances calculated from the same fitting (Figure 10e). The highest cathode capacitance, which represents the largest contact

area between the electron and ion conductors, corresponds to the CCM, hot-pressed at 1.18 MPa, with the lowest cathode charge transfer resistance, lowest total resistance, and best PEMFC performance at current densities ≤ 3.0 A/cm^2. This is followed by the CCM hot-pressed at 7.10 MPa and the CCM hot-pressed at 0.23 MPa. Interestingly, the analysis of anode capacitances—more than five times lower than the cathode capacitances—shows an increasing trend with the hot-pressing pressure.

At lower gas flow rates, polarization studies were conducted to evaluate the effects of expected more pronounced diffusion resistance and pore structural differences under conditions where mass transport limitations become visible. The polarization curves in Figure 10f show minimal performance differences between CCMs prepared at different hot-pressing forces. This lack of disparity can be explained by the interplay between the different resistances and pore structure: the improved pore structure in CCMs produced at lower hot-pressing forces appears to offset the performance losses due to the higher ohmic resistance. Conversely, the reduced ohmic resistance in CCMs prepared at higher hot-pressing forces compensates for any limitations arising from a less favorable pore structure. This dual influence—where structural and respectively resistance-related factors counterbalance each other—accounts for the minimal performance variation observed under lower gas flow rates.

The electrochemical study demonstrates that the impact of the hot-pressing pressure on the catalyst layer performance is highly dependent on the fuel cell's operational conditions. Under high reactant gas stoichiometric coefficients, the differences in cathode charge transfer and diffusion resistances dominate to the ohmic resistance, with the moderate hot-pressing pressure yielding the best performance at current densities ≤ 3 A/cm² due to the lowest ohmic and cathode charge transfer resistances. Conversely, at low stoichiometric coefficients, both pore microstructure and different resistances become relevant. Here, the enhanced pore structure seen at lower hot-pressing pressures does not sufficiently counterbalance the increase in total resistance leading to no significant performance advantage. Consequently, under low stoichiometric coefficients, variations in hot-pressing pressure show minimal impact on the overall performance. This study highlights how microstructural analysis can provide a rational basis for the observed performance variations in fuel cell catalyst layers under different hot-pressing conditions. Such way, the developed methodology offers a robust foundation for future modeling and operando studies to further refine and predict fuel cell behavior under varying operational scenarios.

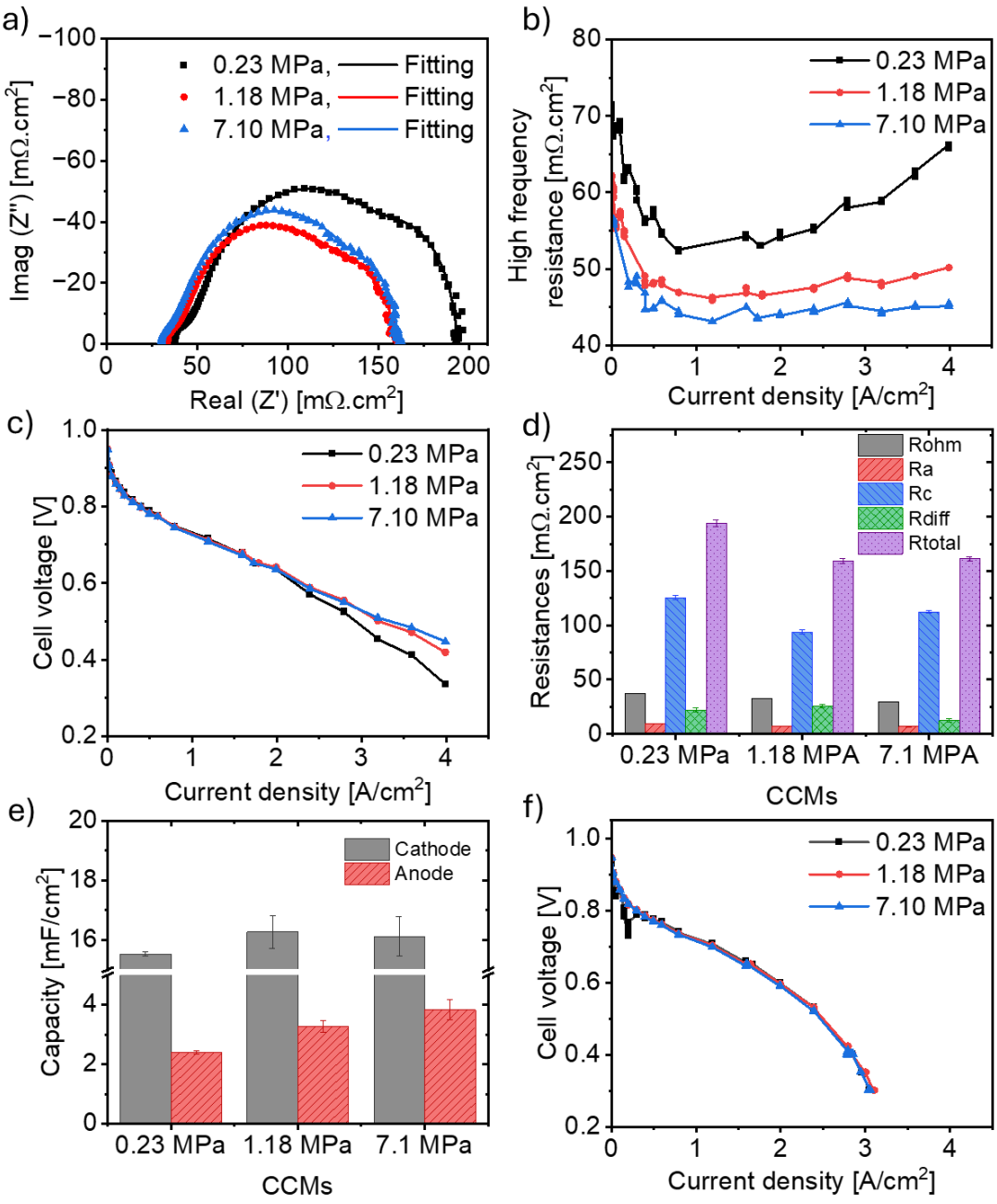

Figure 10: Electrochemical study of catalyst coated membranes prepared by hot-pressing at different pressures. (a) EIS at DC of 2 A/cm², AC perturbation of 0.1 A/cm² and anode/cathode stoichiometric coefficient of 5/5; (b) high frequency resistance study at anode/cathode stoichiometric coefficient of 5/5; (c) polarization curves acquired at anode/cathode stoichiometric coefficient of 5/5; (d) resistances of CCMs at current density 2 A/cm² and stoichiometric coefficient of 5/5; (e) average anode and cathode capacities calculated from the EIS fitting model at 1, 2 and 3 A/cm²; (f) polarization curves acquired at anode/cathode stoichiometric coefficient of 2/2.

4. Conclusion

This study presents a pioneering methodology for investigating catalyst layer microstructures, achieving critical insights into the relationship between process parameters, microstructural properties, and electrochemical performance in CCMs for PEMFCs. Key highlights from this research include the following:

1. We developed a specialized image processing algorithm capable of analyzing cross-sectional images from a non-destructive FIB-SEM device. This algorithm efficiently calculates essential pore characteristics—including porosity, pore sizes, and pore geometry—enabling accurate quantification of microstructural features that are essential for optimizing catalyst layer performance.
2. A comprehensive, multi-scale structural analysis method was established, covering catalyst layer microstructures across a wide range of sizes, from hundreds of micrometers down to tens of nanometers. By combining FIB-SEM image analysis, MIP and carefully chosen microscopy techniques, this method provides a detailed examination of catalyst layer properties, from bulk porosity and pore size distribution to intricate pore geometries. This approach enables a thorough characterization of pore structures and surface roughness across different size regimes.
3. Using our comprehensive analysis method, we successfully linked characteristic features in the pore size distribution from MIP to corresponding physical microstructural attributes visible across various microscopy platforms. This correlation provides a robust framework for interpreting microstructural changes as they occur when production process parameters are changed.
4. A significant finding of this study is the discovery that catalyst layers produced from different dispersions exhibit distinct behaviors under varying hot-pressing pressures. While some dispersions showed predictable densification patterns with reduced porosity under high pressure, others displayed unique responses, such as an unexpected increase in porosity. This attributes to the different drying mechanism that the catalyst layers undergo due to the difference in their A/W ratio. This behavior underscores the influence of dispersion formulation on the microstructural response to hot-pressing, providing insights that are critical for selecting optimal dispersion formulations and processing conditions.
5. The developed analysis methodology enabled a deeper investigation into microstructure-catalyst layer property-performance relationships. By correlating microstructural properties to electrochemical performance, we demonstrated how changes in process parameters, particularly hot-pressing force and dispersion composition, directly impact catalyst layer characteristics. Insights from the image

analysis tool, particularly regarding pore size and geometry alterations, were invaluable in linking process changes to performance variations.

6. Electrochemical testing provided critical insights into how microstructural changes during hot-pressing translate to fuel cell performance under varying operational conditions. At high reactant gas stoichiometric coefficients, cathode charge transfer and ohmic resistance differences dominate, with moderate to higher hot-pressing pressures yielding better performance due to reduced resistances. Under low stoichiometric coefficients, both pore microstructure, accounted by the diffusion resistance, cathode charge transfer and ohmic resistances become influential, but the improved pore structure at lower hot-pressing pressures does not sufficiently offset the higher resistances, resulting in minimal performance gains. This underscores the importance of microstructural analysis in explaining performance variations across different hot-pressing conditions.

In conclusion, the developed multi-scale MIP-microscopy correlative analysis method, complemented by the in-house developed image analysis algorithm, has proven to be a powerful tool for characterizing and optimizing catalyst layer properties, offering detailed insights that are essential for the rational design of high-performance CCMs. Future work should focus on two major aspects. First, improving the developed algorithm to handle 3-dimensional image data will enable a comprehensive 3-dimensional understanding of the pore microstructure. Second, adapting the developed methodology to other electrochemical systems, such as proton exchange membrane electrolyzers, could broaden the application of our findings. This adaptability offers a promising outlook for enhancing the performance and design of various electrochemical systems.

Acknowledgements

This work was financially supported by the Ministry of Economic Affairs, Industry, Climate Action, and Energy of the State of North Rhine-Westphalia through the R2R-CCM project, for which the authors express their gratitude. The authors also extend their appreciation to the collaboration partners, Hydrogen and Fuel Cell Center (ZBT) and Laufenberg GmbH, for their invaluable experimental contributions, as well as the Interdisciplinary Center for Analytics on the Nanoscale (ICAN) for providing analytical measurement support.

Data availability

The data supporting this study will be made available on Zenodo (https://zenodo.org/).

References

[1] F. van der Linden, E. Pahon, S. Morando, D. Bouquain, A review on the Proton-Exchange Membrane Fuel Cell break-in physical principles, activation procedures, and characterization methods, Journal of Power Sources 575 (2023) 233168. https://doi.org/10.1016/j.jpowsour.2023.233168.

[2] K. Sopian, W.R. Wan Daud, Challenges and future developments in proton exchange membrane fuel cells, Renewable Energy 31 (2006) 719–727. https://doi.org/10.1016/j.renene.2005.09.003.

[3] M. Shen, The characteristics of power generation of static state fuel cells, Journal of Power Sources 115 (2003) 203–209. https://doi.org/10.1016/S0378-7753(02)00731-0.

[4] P.T. Yu, W. Gu, J. Zhang, R. Makharia, F.T. Wagner, H.A. Gasteiger, Carbon-Support Requirements for Highly Durable Fuel Cell Operation, in: F.N. Büchi, M. Inaba, T.J. Schmidt (Eds.), Polymer Electrolyte Fuel Cell Durability, Springer New York, New York, NY, 2009, pp. 29–53.

[5] Brian D James, Jennie M Huya-Kouadio, Cassidy Houchins, Daniel A Desantis, Mass Production Cost Estimation of Direct H2 PEM Fuel Cell Systems for Transportation Applications: 2017 Update, Unpublished, 2017.

[6] B.H. Lim, E.H. Majlan, A. Tajuddin, T. Husaini, W.R. Wan Daud, N.A. Mohd Radzuan, M.A. Haque, Comparison of catalyst-coated membranes and catalyst-coated substrate for PEMFC membrane electrode assembly: A review, Chinese Journal of Chemical Engineering 33 (2021) 1–16. https://doi.org/10.1016/j.cjche.2020.07.044.

[7] S.H. Joo, K. Kwon, D.J. You, C. Pak, H. Chang, J.M. Kim, Preparation of high loading Pt nanoparticles on ordered mesoporous carbon with a controlled Pt size and its effects on oxygen reduction and methanol oxidation reactions, Electrochimica Acta 54 (2009) 5746–5753. https://doi.org/10.1016/j.electacta.2009.05.022.

[8] M.K. Debe, Electrocatalyst approaches and challenges for automotive fuel cells, Nature 486 (2012) 43–51. https://doi.org/10.1038/nature11115.

[9] A.A. Gewirth, M.S. Thorum, Electroreduction of dioxygen for fuel-cell applications: materials and challenges, Inorg. Chem. 49 (2010) 3557–3566. https://doi.org/10.1021/ic9022486.

[10] A.J. Appleby, Electrocatalysis of aqueous dioxygen reduction, Journal of Electroanalytical Chemistry 357 (1993) 117–179. https://doi.org/10.1016/0022-0728(93)80378-U.

[11] T. Reshetenko, O. Polevaya, Determination of oxygen mass transport resistance in proton exchange membrane fuel cells with an open flow field architecture, Electrochimica Acta 387 (2021) 138529. https://doi.org/10.1016/j.electacta.2021.138529.

[12] A. Kongkanand, M.F. Mathias, The Priority and Challenge of High-Power Performance of Low-Platinum Proton-Exchange Membrane Fuel Cells, J. Phys. Chem. Lett. 7 (2016) 1127–1137. https://doi.org/10.1021/acs.jpclett.6b00216.
[13] A.Z. Weber, A. Kusoglu, Unexplained transport resistances for low-loaded fuel-cell catalyst layers, J. Mater. Chem. A 2 (2014) 17207–17211. https://doi.org/10.1039/c4ta02952f.
[14] Y. Yoon, Effect of pore structure of catalyst layer in a PEMFC on its performance, International Journal of Hydrogen Energy 28 (2003) 657–662. https://doi.org/10.1016/S0360-3199(02)00156-8.
[15] S. Ghosh, H. Ohashi, H. Tabata, Y. Hashimasa, T. Yamaguchi, Microstructural pore analysis of the catalyst layer in a polymer electrolyte membrane fuel cell: A combination of resin pore-filling and FIB/SEM, International Journal of Hydrogen Energy 40 (2015) 15663–15671. https://doi.org/10.1016/j.ijhydene.2015.09.080.
[16] A. Zhang, G. Zhu, M. Zhai, S. Zhao, L. Zhu, D. Ye, Y. Xiang, T. Tian, H. Tang, Construction of catalyst layer network structure for proton exchange membrane fuel cell derived from polymeric dispersion, J. Colloid Interface Sci. 638 (2023) 184–192. https://doi.org/10.1016/j.jcis.2023.01.132.
[17] G. Doo, S. Yuk, J.H. Lee, S. Choi, D.-H. Lee, D.W. Lee, J. Hyun, S.H. Kwon, S.G. Lee, H.-T. Kim, Nano-scale control of the ionomer distribution by molecular masking of the Pt surface in PEMFCs, J. Mater. Chem. A 8 (2020) 13004–13013. https://doi.org/10.1039/C9TA14002F.
[18] C.-Y. Jung, S.-W. Choi, W.-Y. Choi, C.-W. Hong, V.R. Jothi, S.-C. Yi, Engineering ionomer homogeneously distributed onto the fuel cell electrode with superbly retrieved activity towards oxygen reduction reaction, Applied Catalysis B: Environmental 298 (2021) 120609. https://doi.org/10.1016/j.apcatb.2021.120609.
[19] S.-D. Yim, Y.-J. Sohn, S.-H. Park, Y.-G. Yoon, G.-G. Park, T.-H. Yang, C.-S. Kim, Fabrication of microstructure controlled cathode catalyst layers and their effect on water management in polymer electrolyte fuel cells, Electrochimica Acta 56 (2011) 9064–9073. https://doi.org/10.1016/j.electacta.2011.05.123.
[20] M. Eikerling, Water Management in Cathode Catalyst Layers of PEM Fuel Cells, J. Electrochem. Soc. 153 (2006) E58. https://doi.org/10.1149/1.2160435.
[21] J. Liu, M. Eikerling, Model of cathode catalyst layers for polymer electrolyte fuel cells: The role of porous structure and water accumulation, Electrochimica Acta 53 (2008) 4435–4446. https://doi.org/10.1016/j.electacta.2008.01.033.
[22] S.H. Woo, S. Kim, S. Woo, S.-H. Park, Y.S. Kang, N. Jung, S.-D. Yim, Investigating the effect of solvent composition on ink structure and crack formation in polymer electrolyte membrane fuel cell catalyst layers, Korean J. Chem. Eng. 40 (2023) 2455–2462. https://doi.org/10.1007/s11814-023-1474-3.
[23] J.K. Lee, P. Shrestha, A.M. Hasan, A. Bazylak, 4 Synchrotron X-ray imaging of PEMFCs, in: J. Jankovic, J. Stumper (Eds.), PEM Fuel Cells, De Gruyter, 2023, pp. 113–136.

[24] H. Markötter, R. Alink, J. Haußmann, K. Dittmann, T. Arlt, F. Wieder, C. Tötzke, M. Klages, C. Reiter, H. Riesemeier, J. Scholta, D. Gerteisen, J. Banhart, I. Manke, Visualization of the water distribution in perforated gas diffusion layers by means of synchrotron X-ray radiography, International Journal of Hydrogen Energy 37 (2012) 7757–7761. https://doi.org/10.1016/j.ijhydene.2012.01.141.

[25] H. Xu, S. Nagashima, H.P. Nguyen, K. Kishita, F. Marone, F.N. Büchi, J. Eller, Temperature dependent water transport mechanism in gas diffusion layers revealed by subsecond operando X-ray tomographic microscopy, Journal of Power Sources 490 (2021) 229492. https://doi.org/10.1016/j.jpowsour.2021.229492.

[26] J. Liu, M.R. Talarposhti, T. Asset, D.C. Sabarirajan, D.Y. Parkinson, P. Atanassov, I.V. Zenyuk, Understanding the Role of Interfaces for Water Management in Platinum Group Metal-Free Electrodes in Polymer Electrolyte Fuel Cells, ACS Appl. Energy Mater. 2 (2019) 3542–3553. https://doi.org/10.1021/acsaem.9b00292.

[27] S.H. Akella, E. D, S.S. R S, A. Ahire, N.K. Mal, Studies on structure property relations of efficient decal substrates for industrial grade membrane electrode assembly development in pemfc, Sci. Rep. 8 (2018) 12082. https://doi.org/10.1038/s41598-018-30215-0.

[28] L. Grebener, A. Odungat, Y. Zhu, O. Pasdag, I. Radev, E. Nürenberg, A. Kubina, V. Peinecke, S. Kohsakowski, D. Segets, F. Özcan, Investigation of Fuel Cell Catalyst Dispersion Formulations for Indirect Roll-to-Roll Fabrication of Catalyst Coated Membranes for Proton Exchange Membrane Fuel Cells, 2024.

[29] J. Zhao, H. Liu, X. Li, Structure, Property, and Performance of Catalyst Layers in Proton Exchange Membrane Fuel Cells, Electrochem. Energ. Rev. 6 (2023) 13. https://doi.org/10.1007/s41918-022-00175-1.

[30] H. Giesche, Mercury Porosimetry: A General (Practical) Overview, Part & Part Syst Charact 23 (2006) 9–19. https://doi.org/10.1002/ppsc.200601009.

[31] J. Xie, K.L. More, T.A. Zawodzinski, W.H. Smith, Porosimetry of MEAs Made by "Thin Film Decal" Method and Its Effect on Performance of PEFCs, J. Electrochem. Soc. 151 (2004) A1841. https://doi.org/10.1149/1.1796991.

[32] M. Uchida, Y. Aoyama, N. Eda, A. Ohta, Investigation of the Microstructure in the Catalyst Layer and Effects of Both Perfluorosulfonate Ionomer and PTFE-Loaded Carbon on the Catalyst Layer of Polymer Electrolyte Fuel Cells, J. Electrochem. Soc. 142 (1995) 4143–4149. https://doi.org/10.1149/1.2048477.

[33] N. Kumano, K. Kudo, A. Suda, Y. Akimoto, M. Ishii, H. Nakamura, Controlling cracking formation in fuel cell catalyst layers, Journal of Power Sources 419 (2019) 219–228. https://doi.org/10.1016/j.jpowsour.2019.02.058.

[34] P. Quarz, N. Zimmerer, P. Scharfer, W. Schabel, About drying phenomena of fuel cell and electrolyzer CCM inks: Selectivity of the evaporation of 1-propanol/water mixtures, Fuel Cells 24 (2024) 108–121. https://doi.org/10.1002/fuce.202300252.

[35] J. Farmer, B. Duong, S. Seraphin, S. Shimpalee, M.J. Martínez-Rodríguez, J.W. van Zee, Assessing porosity of proton exchange membrane fuel cell gas diffusion layers

by scanning electron microscope image analysis, Journal of Power Sources 197 (2012) 1–11. https://doi.org/10.1016/j.jpowsour.2011.08.064.
[36] T. Suzuki, H. Tanaka, M. Hayase, S. Tsushima, S. Hirai, Investigation of porous structure formation of catalyst layers for proton exchange membrane fuel cells and their effect on cell performance, International Journal of Hydrogen Energy 41 (2016) 20326–20335. https://doi.org/10.1016/j.ijhydene.2016.09.078.
[37] J.-C. Lin, C.-M. Lai, F.-P. Ting, S.-D. Chyou, K.-L. Hsueh, Influence of hot-pressing temperature on the performance of PEMFC and catalytic activity, J Appl Electrochem 39 (2009) 1067–1073. https://doi.org/10.1007/s10800-008-9758-1.

Supplementary Information

Multiscale analysis method

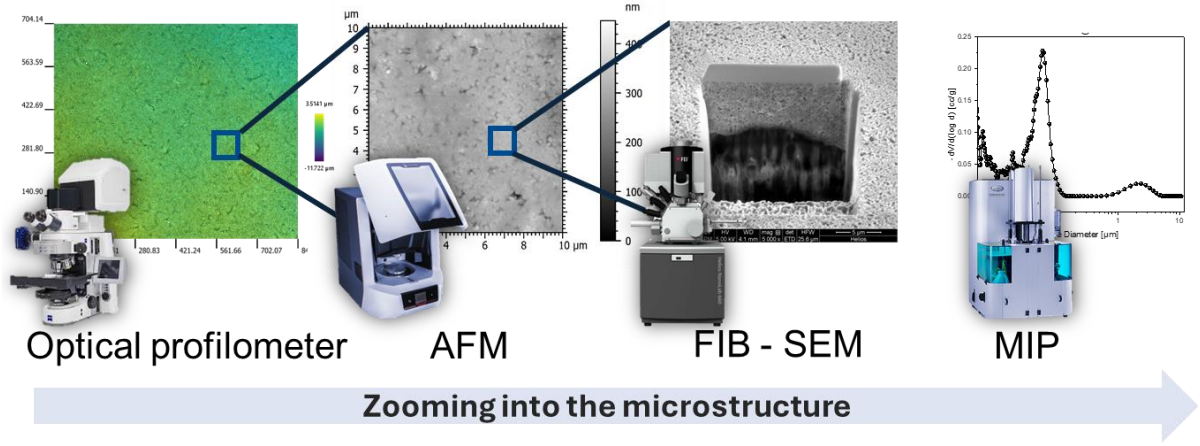

Supplementary Figure S1: Schematic representation of the multi-scale analysis method developed for studying the microstructural features of catalyst layers across different size regimes.

FIB-SEM cross-section imaging

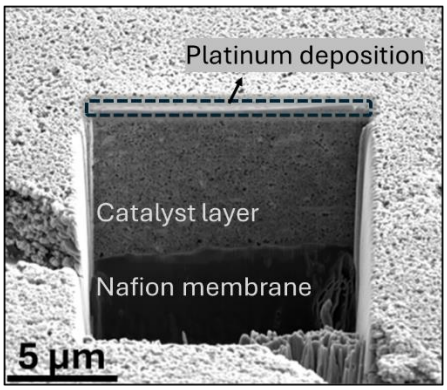

Supplementary Figure S2: The rectangular hole (15 µm x 15 µm) created on the surface of the catalyst layer using focused ion beams in the FIB-SEM device. The protective platinum deposition and the catalyst layer-membrane interface can be seen in the picture.

Results

Mercury intrusion porosimetry

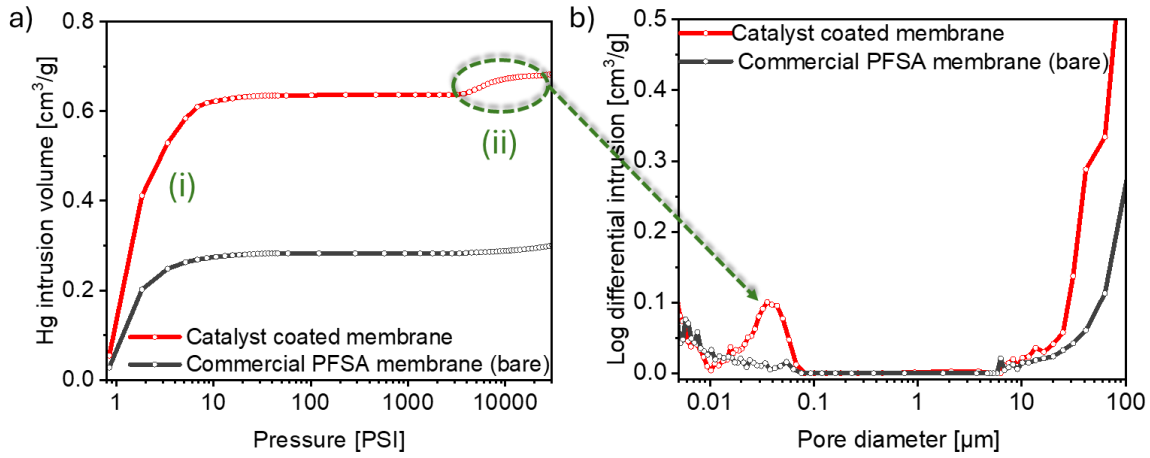

Supplementary Figure S3: Mercury intrusion porosimetry (MIP) data of half CCMs and uncoated PFSA membranes. (a) Mercury intrusion volume profiles; (b) pore size distribution derived from the MIP data.

Electrochemical analysis

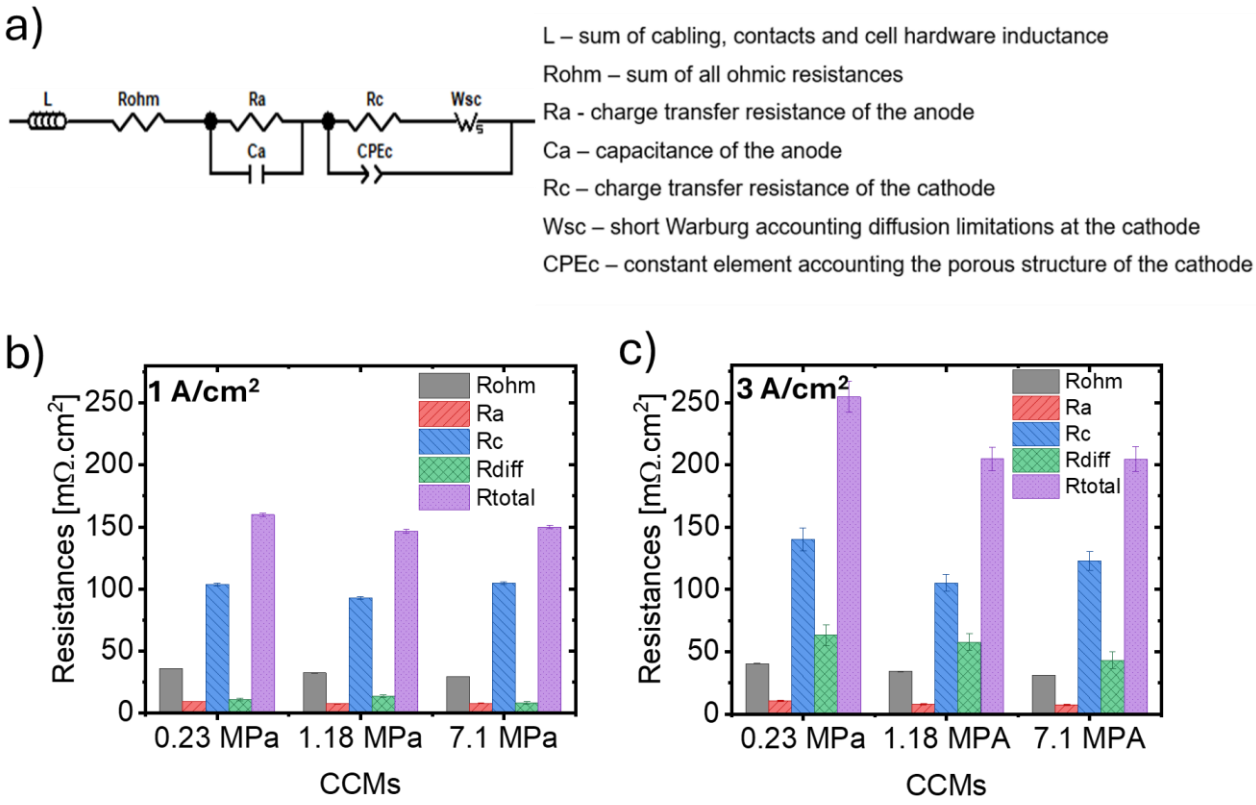

Supplementary Figure S4: Electrochemical analysis of CCMs. (a) EIS fitting model; resistances of CCMs prepared under different hot-pressing pressure at stoichiometric coefficient of 5/5 and current densities of (b) 1 A/cm^2 and (c) 3 A/cm^2.